



Albedo-Ice regression method for determining ice water content of Polar Mesospheric Clouds using ultraviolet observations from space

Gary E. Thomas¹, Jerry Lumpe², Charles Bardeen³ and Cora E. Randall^{1,4}

¹Laboratory for Atmospheric and Space Physics, University of Colorado Boulder, Boulder, Colorado, USA

²Computational Physics, Inc., Boulder, Colorado, USA

³National Center for Atmospheric Research, Boulder, Colorado, USA

⁴Department of Atmospheric and Oceanic Sciences, University of Colorado Boulder, Colorado, USA

Correspondence to: Gary E. Thomas (thomas@lasp.colorado.edu)



1 **Abstract.** High spatial-resolution images of Polar Mesospheric Clouds (PMC) from a
2 camera array onboard the Aeronomy of Ice in the Mesosphere Satellite have been
3 obtained since 2007. The Cloud Imaging and Particle Size Experiment (CIPS) detects
4 scattered ultraviolet (UV) radiance at a variety of scattering angles, allowing the
5 scattering phase function to be measured for every image pixel. With well-established
6 scattering theory, the mean particle size and ice water content (IWC) are derived. In
7 the nominal mode of operation, approximately seven scattering angles are measured
8 per cloud pixel. However, because of a change in the orbital geometry in 2016, a new
9 mode of operation was implemented such that one, or at most two, scattering angles
10 per pixel are now available. Thus particle size and IWC can no longer be derived from
11 the standard CIPS algorithm. The Albedo-Ice Regression (AIR) method was devised to
12 overcome this obstacle. Using data from both a microphysical model and from CIPS in
13 its normal mode, we show that the AIR method provides sufficiently accurate average
14 IWC so that PMC IWC can be retrieved from CIPS data into the future, even when
15 albedo is not measured at multiple scattering angles. We also show from the model
16 that 265nm UV scattering is sensitive only to ice particle sizes greater than about 20-
17 25 nm in (effective) radius, and that the operational CIPS algorithm has an average
18 error in retrieving IWC of $-13 \pm 17\%$.

19 **1 Introduction**

20 Polar Mesospheric Clouds (known as noctilucent clouds in the ground-based
21 literature) have been studied for over a century from high-latitude ground
22 observations, but only since the space age have we understood their physical nature,
23 as water-ice particles occurring in the extremely cold summertime mesopause region.
24 Their seasonal and latitudinal variations have now been well documented (DeLand et
25 al., 2006). Interest in these clouds ‘at the edge of space’ has been stimulated by
26 suggestions that they are sensitive to global change in the mesosphere (Thomas et al.,
27 1989). This expectation has been supported recently by a time series analysis of Solar
28 Backscattered Ultraviolet measurements of PMC (Hervig et al., 2016) and by model
29 calculations (Lübken et al., 2018).

30 The Aeronomy of Ice in the Mesosphere satellite (AIM) (Russell et al., 2009) was
31 designed to provide a deeper understanding of the basic processes affecting PMC,
32 through remote sensing of both the clouds and their physical environment
33 (temperature, water vapor, and meteor smoke density, among other constituents).
34 One of the two active experiments on board AIM is a camera array, the Cloud Imaging
35 and Particle Size (CIPS) experiment, which provides high spatial resolution images of
36 PMC (McClintock et al., 2009). CIPS measures scattered ultraviolet (UV) sunlight in the
37 nadir in a spectral region centered at 265 nm, where ozone absorption allows the
38 optically-thin ice particles to be visible above the Rayleigh scattering background



39 issuing from the ~50-km region (Rusch et al., 2009; Bailey et al., 2009). Because of its
40 wide field of view and 43-second image cadence, CIPS views a cloud element multiple
41 times in its sun-synchronous orbital passage over the polar region, thus providing
42 consecutive measurements of the same location at multiple (typically seven)
43 scattering angles (SA). Together with scattering theory, the brightness of the cloud
44 (albedo) at multiple angles provides constraints needed to estimate the mean ice
45 particle size (Lumpe et al., 2013). From the particle size and albedo measurements,
46 the ice water content is calculated for each cloud element (7.5 x 7.5 km² in the most
47 recent CIPS retrieval algorithm). However, over time, the AIM orbit plane has drifted
48 from its nominal noon-midnight orientation to the point where the satellite is
49 currently operating in a terminator orbit. Responding to this altered geometry and the
50 desire to broaden the scope of AIM, new measurement sequences were implemented
51 to provide observations of the entire sunlit hemisphere, rather than just the
52 summertime high-latitude region. Because the total number of images per orbit is
53 fixed by data storage limitations, a new mode (the ‘continuous imaging mode’) of
54 observations, with a reduced three-minute image cadence, was implemented in
55 February 2016. The present sampling in a single Level 2 pixel contains many fewer
56 scattering angles (often only one). To maintain consistency in the study of inter-
57 annual variations of PMC, this necessitates a revised method of retrieving ice water
58 content (IWC) where only a single albedo measurement is available. IWC is a valuable
59 measure of the physical properties of PMC since it largely removes the effects of
60 scattering-angle geometry, is a convenient PMC climate variable when averaged over
61 season, and can be used in comparing with contemporaneous measurements of PMC
62 that use different observational techniques.

63 The Albedo-Ice Regression (AIR) method was developed to fill the need to retrieve
64 PMC IWC with only a single measurement of albedo. Based on the simple notions that
65 both albedo and IWC depend linearly upon the ice-particle column density, multiple
66 linear relationships are established between IWC and cloud directional albedo,
67 depending upon scattering angle. The regressions are derived from three data
68 sources: (1) the Specified Dynamics version of the Whole Atmosphere Community
69 Climate Model (SD-WACCM) combined with the Community Aerosol and Radiation
70 Model for Atmospheres (CARMA); (2) CIPS data for the years 2007-2013, when
71 multiple scattering angles were available to derive IWC; and (3) Solar Occultation For
72 Ice Experiment (SOFIE), which provides IWC and particle sizes. These three sources
73 provide many thousands of albedo-IWC-particle size combinations, from which the
74 AIR regressions are derived. Although the AIR method may be inaccurate for a single
75 retrieval of IWC, averages over many observations result in close agreement as the
76 number of data points increases. The utility of AIR thus depends upon the availability



77 of large data sets that apply to roughly the same atmospheric conditions. For example,
78 we will show CIPS results for July and January averages for ascending and descending
79 portions of the orbit.

80 In this paper we first describe the theoretical framework relating the scattered
81 radiance to mesospheric ice particles. It is desirable to use model data to test the AIR
82 method, without the complications of cloud heterogeneity and viewing geometry. We
83 utilized a first-principles microphysical model that accurately simulates large numbers
84 of cloud properties (number density and particle size distribution). The processes
85 treated by the model include meteor ‘smoke’ nucleation, growth, and sedimentation,
86 occurring in a saturated environment at density and temperature conditions provided
87 by the main global climate model (Bardeen et al., 2010). Several runs for one-day and
88 multiple-day periods during summer solstice conditions for solar conditions applying
89 to 1995 were analyzed. Cloud radiances (albedos) at 265 nm were calculated for the
90 SA range encountered by the CIPS experiment. We chose a set of cloud simulations to
91 derive a single set of two AIR coefficients through linear regression. The accuracy of
92 the AIR approximation was then tested on the same data, and on other model runs,
93 using averages as a function of SA, and increasing IWC threshold values. Thresholding
94 is necessary to account for the fact that different measurement techniques have
95 different detection sensitivities. This is not a signal/noise issue, rather the ability to
96 discriminate PMC against a background that is usually larger than the PMC signal
97 itself. We show in particular how seasonal means of IWC can be derived from Solar
98 Backscatter Ultraviolet Spectrometer (SBUV) radiance data, without the need to
99 derive particle size.

100 Having tested the technique for model data, we use the same approach with real-life
101 PMC data collected from CIPS in the normal pre-2016 operating mode. This mode
102 provided scattering angles needed to define an ice scattering phase function, from
103 which mean particle size was derived based on assumed properties of the underlying
104 size distribution (Lumpe et al., 2013). The regressions were run for a period of 40 days
105 in each of four seasons, each comprising millions of separate cloud measurements,
106 and from both summertime hemispheres. The results were combined into a single set
107 of AIR coefficients, and again the AIR technique was tested on monthly averages.
108 These averages were constructed over all years of nominal spacecraft operations
109 (2007-2013 in the northern hemisphere, and 2007-8 through 2013-14 in the southern
110 hemisphere). Note that testing the accuracy of the AIR technique during the nominal
111 mission period allows the method to be used even during the ‘continuous imaging
112 mode’ of CIPS operation.

113 We then employed highly-accurate data from SOFIE for ice column density and mean
114 particle size. Since the SOFIE technique uses near-IR solar extinction, it is necessary to



115 derive scattered radiances from the same algorithm used by CIPS. This exercise was
 116 performed primarily to test whether the derived AIR results are broadly consistent
 117 with those derived from the model and CIPS.

118 After describing the AIR method, we discuss briefly the application of the method to
 119 a third contemporaneous experiment, the SBUV satellite experiment, which has in
 120 common the same limitations as CIPS in its continuous-imaging mode, namely that
 121 measurements of nadir albedo are made at a single scattering angle. This has already
 122 resulted in a publication (DeLand and Thomas, 2015) where we provided a time series
 123 of PMC IWC from the AIR method extending back to the first SBUV experiment in
 124 1979.

125 2 Theoretical Basis

126 Here we provide a brief overview of the theoretical basis of the IWC retrieval
 127 technique, referring to previous publications for more detail (Thomas and McKay,
 128 1985; Rusch et al., 2009; Bailey et al., 2009, Lumpe et al., 2013). The basic
 129 measurement is PMC cloud radiance $I(\Phi, \theta)$ where Φ is the scattering angle (angle
 130 between the sun and observation vectors) and θ is the view angle, which is the angle
 131 subtended by the nadir and observation direction, measured from the point of
 132 scattering. Since the ice layer is optically thin, and secondary scattering is negligible,
 133 the albedo is described by first-order scattering. The ratio of scattered (detected)
 134 radiance to the incoming solar irradiance F_λ is the albedo A_λ , where

$$A_\lambda(\Phi, \theta) = I_\lambda(\Phi, \theta) / F_\lambda = \sec \theta \int_{z_b}^{z_t} dz' \int_{r_{\min}}^{r_{\max}} dr' \sigma_\lambda(r, \Phi) n(r', z') \quad (1)$$

135 Here z' and r' are the height and particle radius variables, and z_b and z_t define the
 136 height limits of the ice layer, with the majority of the integrand extending between 83
 137 and 85 km. r_{\min} and r_{\max} are particle radii which span the particle size regime
 138 responsible for scattering (from ~ 20 nm to ~ 150 nm). σ_λ is the monochromatic
 139 scattering cross-section ($\text{cm}^2\text{-sr}^{-1}$) at wavelength λ and scattering angle Φ .
 140 $n(r', z') dr' dz'$ is the number density of ice particles (cm^{-2}) in the ranges $r', r'+dr'$ and
 141 $z', z'+dz'$. For CIPS measurements, each camera has a finite bandpass, centered at 265
 142 nm, and is characterized by a function R_λ with an effective width of 10 nm
 143 (McClintock et al., 2009). The albedo derived from this instrument is given by

$$A_\lambda(\Phi, \theta) = \sec \theta \int d\lambda' R_\lambda \int_{z_t}^{z_b} dz' \int_{r_{\min}}^{r_{\max}} dr' \sigma_\lambda(r, \Phi) n(r', z') \quad (2)$$



144 In the model, the ice particles are assumed spherical, but the scattering theory should
 145 take account of the non-spherical nature of ice crystals. The best agreement of theory
 146 with near-IR mesospheric ice extinction occurs for a randomly rotating oblate-
 147 spheroid shape, of axial ratio two (Hervig and Gordley, 2010). This shape is assumed
 148 in the calculation of σ_λ , which is accomplished through a generalization of Mie-Debye
 149 scattering theory, the T-matrix method (Mishchenko and Travis, 1998). The radius in
 150 the T-matrix approach is defined as the radius of the volume-equivalent sphere. In the
 151 model calculations, we will ignore the view angle effect. In the reported CIPS data,
 152 the $\sec\theta$ factor is applied to the reported albedos, so that A always refers to the nadir
 153 albedo ($\theta = 0$).

154 The ice water content (IWC) is the integrated mass of ice particles over a vertical
 155 column through the ice layer. Its definition is

$$IWC = \rho \int_{z_b}^{z_t} dz' \int_{r_{\min}}^{r_{\max}} dr' (4\pi/3) r'^3 n(r', z') \quad (3)$$

156 ρ denotes the density of water-ice at low temperature (0.92 g-cm^{-3}). Anticipating the
 157 results of this study that IWC is linearly related to the column density of ice particles,

158 $N = \int dr' \int dz' n(r, z')$, we explore the physical basis of this result. As first pointed out
 159 by Englert and Stevens (2007), such a relationship exists for certain SA values, for
 160 which $\sigma \sim r^3$, in which case it is easily seen that Eq. (2) is proportional to IWC.
 161 However, we find that a linear approximation is valid for a much wider range of
 162 scattering angles. To understand this result, we imagine that all particles have the
 163 same radius, so that $n = n_c \delta(r - r_c)$, where δ is the Dirac δ -function. Then Eqs. (1)
 164 and (3) ‘collapse’ to simpler results,

$$A_\lambda(\Phi, 0) = \sigma_\lambda(r_c, \Phi) N(r_c), \quad IWC(r_c) = \rho V(r_c) N(r_c) \quad (4)$$

165 Here $N(r_c) = n_c \Delta z$ where Δz is the effective vertical thickness of the ice layer.
 166 Eliminating the column density $N(r_c)$, the ice water content is written

$$IWC(r_c) = \rho V(r_c) A(\Phi, 0) / \sigma_\lambda(r_c, \Phi) \quad (5)$$

167 $V(r_c)$ denotes the particle volume. Thus in this special case, $IWC(r_c) \sim A_\lambda(\Phi, 0)$. A
 168 superposition of the effects of all participating particle sizes will exhibit a similar
 169 proportionality. When $IWC(r)$ is integrated over all r , the contributions from each
 170 size are straight lines, each having different intercepts and slopes.



171 As previously discussed, the value of the AIR method is in evaluating *average* IWC
172 (denoted by $\langle \text{IWC} \rangle$) over many albedo observations made at numerous scattering
173 angles. The accuracy of the method should be assessed on this basis, not on how well
174 an individual albedo measurement yields the correct value of IWC. An important issue
175 is the differing detection thresholds for IWC among the various experiments. In the
176 case of the scattered-light experiments, the detection threshold depends upon how
177 well the cloud radiance data can be separated from the bright Rayleigh-scattered
178 background. The CIPS experiment retrieval method relies upon high spatial resolution
179 over a large field of view, and the differing scattering-angle dependence of PMC and
180 the Rayleigh-scattering background (Lumpe et al., 2013). The SBUV retrieval relies
181 upon differing wavelength-dependence of PMC and background, but primarily on the
182 PMC radiance residuals being higher (2 sigma) than fluctuations from a smoothly-
183 varying sky background (Thomas et al., 1991; DeLand and Thomas, 2015). The AIM
184 SOFIE method is very different, being a near-IR solar extinction measurement in
185 multiple wavelength bands. SOFIE can detect much weaker clouds than either CIPS or
186 SBUV. Particle radii values as small as 10 nm can be retrieved from the SOFIE data
187 (Hervig et al., 2009). To compare the various experiments, it is necessary to ‘threshold’
188 the data from more sensitive experiments with a cutoff value of IWC.

189 In the next three sections, we present the AIR results from the model, CIPS and SOFIE,
190 using averages over many cloud occurrences. It is not our intention to compare the
191 different thresholded data sets to one another (this task will be relegated to a
192 separate publication), but to illustrate how even measurements made at a single
193 scattering angle (e.g., SBUV) can yield averaged IWC values that are sufficiently
194 accurate to assess variations in daily and seasonal averages. These variations are of
195 crucial value to determining solar cycle and long-term trends in the atmospheric
196 variables (mainly temperature and water vapor) that control ice properties in the cold
197 summertime PMC region. We examine the accuracy of AIR through simulations of
198 scattered radiance from the model, and from CIPS and SOFIE data. Since these data
199 sources yield particle radii, they can provide both the ‘actual’ and approximate values
200 of IWC from the regression formulas. Hervig and Stevens (2014) used the spectral
201 content of the SBUV data to provide limited information on particle size. Together
202 with the albedos themselves, they used this information to derive seasonally-
203 averaged ice water content. They showed that the variation of mean particle size over
204 the 1979-2013 time period was relatively low (standard deviation of ± 1 nm). They
205 also found a very small systematic increase with time, as discussed in Sect. 3.

206 **2. 1 Model Results**

207 Using a microphysical model as a reference source of IWC ‘data’ is useful, in the
208 following ways: (1) in contrast to the CIPS and SOFIE retrieval algorithms, no artificial



209 assumptions are needed concerning the size distribution of ice particles; (2) radiance
210 and IWC may be calculated accurately, so that effects of cloud inhomogeneity are
211 absent; and (3) limitations due to background removal are absent. In addition, to gain
212 insight into the accuracy of the AIR approach, it is sufficient to work with
213 monochromatic radiance at the central wavelength of the various passbands. The
214 integrations of Eqs. (1) and (3) were approximated by sums over 1-nm increments of
215 radius, and over all sub-layers within the model ice cloud (a typical ice layer is several
216 km thick.). The model height grid is variable, being highest in the saturated region
217 where the smallest layer thickness is 0.26 km (see Bardeen et al., 2010 for more
218 details). We then performed the linear regression for SA values over which CIPS
219 observations are made.

220 Figure 1 displays the regressions for six scattering angles, and 2514 individual model
221 clouds. The units of IWC are $\text{g}\cdot\text{km}^{-2}$, or $\mu\text{g}\cdot\text{m}^{-2}$, which are commonly used in the
222 literature. Each plot is divided into two groups according to the effective radii r_{eff} for
223 each cloud. r_{eff} is defined in the literature (Hansen and Travis (1974) as

$$r_{\text{eff}} = \int dr' n(r') r'^3 / \int dr' n(r') r'^2 \quad (6)$$

224 Figure 1 clearly illustrates that particle size contributes to the ‘scatter’ from the linear
225 fits. It also shows the existence of a non-zero intercept of IWC vs albedo. The non-zero
226 intercept was at first surprising since we expected that for an albedo of zero, IWC
227 should also be zero. In fact, we found that the linear relationship breaks down for very
228 small albedo, and the points in the plot narrow down as $A_\lambda \rightarrow 0$ (not shown). In albedo
229 units of 10^{-6}sr^{-1} (hereafter referred to as 1 G) this departure from linearity occurs for
230 $A < 1 \text{ G}$ and $\text{IWC} < 10 \text{ g}/\text{km}^{-2}$, conditions which fortunately are below the sensitivity
231 threshold of CIPS and SBUV, and therefore unimportant for our purposes. For more
232 sensitive detection techniques, this limitation must be kept in mind. A limitation of
233 the present model (not necessarily all models) is that it does not simulate the largest
234 particles in PMC and the largest values of IWC, as seen in both AIM SOFIE and CIPS
235 experiments. The largest model IWC value is $180 \text{ g}\cdot\text{km}^{-2}$ and the largest effective
236 radius is 66 nm, whereas CIPS and SOFIE find particle radii up to 100 nm and IWC up
237 to $300 \text{ g}\cdot\text{km}^{-2}$. This limitation is irrelevant for the AIR CIPS results (to be discussed),
238 but could limit the application of the AIR technique to SBUV data. In Sect. 3 we will
239 return to the issue of the AIR accuracy, as applied to SBUV data.

240 We chose to use averages for the entire model run, which includes different latitudes,
241 longitudes, and UT, but the data can be subset in many different ways. It is certainly
242 preferable in data sets to choose a small time and space interval over which
243 temperature and water vapor are not expected to vary, but this is not necessary for



244 the model. All that we ask of the model is whether the AIR results provide an accurate
 245 estimate of $\langle IWC \rangle$, taken over the ensemble of model cloud albedos calculated at a
 246 variety of scattering angles.

247 As discussed above, we are also interested in the accuracy of AIR in the thresholded
 248 data, that is, how AIR represents $\langle IWC \rangle$ in comparisons of data sets with varying
 249 detection sensitivities to PMC. Figure 2 displays the error in the ensemble-average
 250 (2488 model clouds) as a function of the IWC threshold and scattering angle. Despite
 251 the large data scatter from the linear fit shown in Fig. 1, the averaging removes almost
 252 all the influence of the ‘random error’. In this case, the overall error is less than 3%.
 253 The influence of particle size is of course not a random error, but acts like one in the
 254 averaging process. However, the AIR coefficients also depend weakly upon the mean
 255 effective radius, defined in Eq. (6) for a single cloud, which varies from one latitude to
 256 another and from year to year. The effect of variable r_{eff} on the AIR error is discussed
 257 in Section 3.

258 2.2 AIR Results from CIPS

259 A detailed description of the Version 4.20 CIPS algorithm, together with an error
 260 analysis of individual cloud observations, was presented in Lumpe et al. (2013). Here
 261 we describe only what is necessary to understand how IWC is derived from the data.
 262 Even though an accurate determination of the scattering-angle dependence of
 263 radiance (often called the scattering phase function) is obtained by seven
 264 independent measurements, this does not fully define the distribution of particle
 265 sizes. Instead, additional constraints need to be introduced to derive the mean
 266 particle size. The particles are assumed to be the same oblate-spheroidal shape as
 267 defined for the model calculations, and to have a Gaussian size distribution (see eq.
 268 11 in Rapp and Thomas (2006). A relationship between the Gaussian width s and the
 269 mean particle radius r_m is derived from a relationship found in vertically-integrated
 270 lidar data (Baumgarten et al., 2010). The net result is that two parameters, the mean
 271 particle size and the Gaussian width, are retrieved from a given scattering phase
 272 function. However, there is only one independent variable, since the two are related
 273 by $s(r_m)$. Thus Eq. (3) simplifies to

$$IWC = \rho V(r_m) A(\Phi = 90^\circ, 0) / \sigma_\lambda(r_m, \Phi) \quad (7)$$

274 V denotes the mean ice particle volume evaluated at r_m . A refers to the retrieved
 275 albedo, corrected to view angle $\theta = 0$ and interpolated to scattering angle $\Phi = 90^\circ$.
 276 Note the resemblance of Eq. (7) to Eq. (5). $A(\Phi = 90^\circ, 0)$, along with r_m and IWC
 277 are products reported in the CIPS PMC data base, found at
 278 (<http://lasp.colorado.edu/aim/>). $\sigma_\lambda(r_m, \Phi = 90^\circ)$ is the mean scattering cross-



279 section, integrated over the assumed Gaussian distribution with mean radius r_m and
280 distribution width, s .

281 Before discussing the AIR results, we first apply the CIPS algorithm to the model data
282 to test how well it works on a set of realistic particle sizes. As mentioned earlier, UV
283 measurements of ice particles are not sensitive to particle radii $< 20\text{-}25$ nm. We
284 applied the CIPS algorithm to 6672 model clouds, using seven scattering-angle points,
285 spanning the range $50^\circ\text{-}150^\circ$ (the results are insensitive to the values chosen). We
286 then calculated the % difference between the exact model calculation of IWC and the
287 simulated CIPS retrieved IWC for every model cloud. Figure 3 shows the result as a
288 function of $A(\Phi = 90^\circ)$. The mean difference and standard deviation for two model
289 days is $-13 \pm 17\%$. With the caveat that not all ice is retrieved, only a large subset of
290 CIPS IWC data have an acceptable accuracy (an average of 84% of the modelled ice
291 mass is contained in particles with radii exceeding 23 nm). We note that IWC in the
292 model used to derive the AIR approximation refers to *all* particle sizes.

293 The procedure for deriving AIR coefficients from the CIPS data is as follows: (1)
294 Regression coefficients were derived from data pertaining to 0-40 days from summer
295 solstice (day from solstice, DFS=0 to 40) on every third orbit. This meant that ~ 200
296 orbits per season were used. The regression analysis was performed on four years of
297 data (2010-2013). The data were binned in 5-degree SA bins and only the best quality
298 pixels with six or more points in the phase function were used; (2) Data from each
299 northern and southern summer season were treated separately. The coefficients and
300 standard deviations of the fit were then interpolated to a finer SA grid from 22° to
301 180° in increments of 1° ; (3) The coefficients from each hemisphere were averaged,
302 and these coefficients were then used to create an AIR IWC data base, to accompany
303 the normal CIPS products. As previously shown, the AIR data applies to the ice mass
304 of 'UV-visible' clouds, not to their total ice mass.

305 We emphasize that using the AIR data is unnecessary for seasons prior to the northern
306 summer season of 2016 – however the AIR data have great importance since that time
307 because the observing mode was changed, resulting in measured phase functions that
308 contain many fewer (and often only one) scattering angles. As illustrated in Fig. 4, it is
309 trivial to infer both IWC and $A(90^\circ)$ from a single measurement of albedo. This
310 alternative 90-deg albedo value, ALB_AIR, is now included along with IWC AIR in the
311 CIPS Level 2 data files. Fig. 5 shows the AIR results for monthly-averaged IWC (July and
312 January) compared to the same averages of the more accurate results from the
313 operational (OP) retrieval described in Lumpe et al. (2013). The data have been
314 separated into different hemispheres, and into ascending and descending nodes of
315 the sun-synchronous orbit, and apply to the years of the nominal operating mode. The
316 ALB_AIR results are systematically higher than the operationally retrieved 90-deg



317 albedo, whereas there is no consistent bias in the IWC (AIR) value compared to the
318 operational product. However, for both quantities the interannual changes between
319 the AIR and OP results agree very well. This is reflected in the very high correlation
320 coefficients of the two sets of values. A more stringent test of the AIR method comes
321 from daily values of CIPS IWC. Shown in Figs. 6 and 7 are polar projections of IWC (AIR)
322 and the more accurate operational IWC data product. These ‘daily daisies’ are taken
323 from overlapping orbit strips pertaining to 28 June of two different years. Figure 6
324 shows data from 2012, when CIPS was still in normal mode, and the AIR result shows
325 remarkable agreement with the operational IWC data. By 2016 (see Figure 7) CIPS is
326 in continuous imaging mode and the standard IWC retrieval is limited due to the
327 scarcity of pixels with three or more scattering angles. Here the AIR approach is clearly
328 superior and does a good job of filling in the polar region where CIPS detects high-
329 albedo clouds. The differences in patterns are due primarily to variations of particle
330 size, rather than errors in the AIR method.

331 AIR accuracy can also be tested in the study of latitudinal variations. Figure 8
332 compares daily-averaged IWC from the CIPS Level 3C data, for both the standard and
333 AIR algorithms, for the Northern Hemisphere 2011 season. It is clear that AIR is
334 adequate even for 24-h averages. For example, it is capable of defining the beginning
335 and ending of the PMC season, a metric that has valuable scientific value (e.g., Benze
336 et al., 2012)

337 **2.2 Results from SOFIE**

338 A third independent data set of IWC and particle size is available from the AIM SOFIE
339 experiment. SOFIE provides very accurate values of IWC, through precise near-IR
340 extinction measurements, independent of particle size. It assumes the same Gaussian
341 distribution of particle sizes as CIPS, so that the reported value of mean particle radius
342 r_m is consistently defined. SOFIE data are useful to investigate the extent to which the
343 AIR approximation can be applied to an independent data set. To do so, it is necessary
344 to calculate 265-nm albedo at various SA values, given the values of r_m , ice column
345 density N from the data base, and the mean cross-section $\sigma_\lambda(r_m, \Phi)$. The latter
346 quantity is averaged over the assumed Gaussian distribution. The equation for the
347 albedo is

$$A_\lambda(\Phi, 0) = \sigma_\lambda(r_m, \Phi)N \quad (8)$$

348 Given $A_\lambda(\Phi, 0)$ and IWC for each PMC measurement (one occultation per orbit), we
349 can once again perform regressions and find AIR coefficients for the SOFIE data set.
350 The comparison of AIR results from all three data sets is shown in Fig. 9, where the



351 constant term C is the y-intercept and S is the slope in the AIR regression
352

$$IWC(AIR) = C(\Phi) + S(\Phi) * A(\Phi, 0) \quad (9)$$

353 Figure 10 displays the results from the three data sets, expressed as contour plots of
354 AIR-derived IWC as functions of SA and Albedo. This comparison shows that the three
355 sets of IWC resemble one another far better than would be anticipated from the AIR
356 coefficients in Fig. 9, where the constant coefficient differs significantly between data
357 sets. Since the result of the regression in yielding IWC is more significant than the
358 coefficients themselves, the comparisons of Fig. 10 are the more appropriate
359 diagnostic. The fact that the IWC derived from AIR is more accurate than would be
360 expected from the differing coefficients is due to the fact that the errors of the
361 constant and slope coefficients are anti-correlated. The agreement between the three
362 results will be even better when taken over a large data set with variable SA and
363 albedo. The comparisons of IWC from different satellite experiments as a function of
364 year and hemisphere will be the subject of a separate publication.

365 Figure 11 shows that the regressions with AIM SOFIE data obey a linear relationship
366 between IWC and albedo for IWC <220 g-km⁻², but for SA values <90°, AIR
367 overestimates IWC by up to 15%, depending upon the SA. For SA=100° the regressions
368 are still linear up to 300 g-km⁻², values above which are seldom encountered in the
369 data.

370 2.3 SBUV data

371 The AIR coefficients from the model have been used by DeLand and Thomas (2015) to derive
372 mean IWC from SBUV data, which spans the largest time interval of any satellite data set
373 (1979-present). The 273 nm wavelength used in the SBUV Version 3 analysis is sufficiently
374 close to the effective wavelength of the broader passband of the CIPS cameras (Benze et al.,
375 2009) that the same coefficients may be applied to both data sets. The accuracy of the average
376 IWC results was estimated by removing half the data from an entire season and comparing
377 the two results. For a highly-populated region (more than 1000 clouds per season at latitudes
378 higher than 70°), the changes in IWC were $\pm 3 - 5$ g-km⁻². For a less populated region (50° –
379 64° latitude) where there were many fewer clouds (<50), the changes were larger, $\pm 5 - 10$
380 g-km⁻². Even the larger errors are sufficiently small for intercomparison of SBUV and
381 contemporaneous PMC measurements. Figure 12 shows a comparison of SBUV IWC, using
382 the model AIR coefficients, to the results of a more accurate determination of IWC derived
383 from particle size determinations using SBUV spectral information (Hervig and Stevens, 2014).
384 The comparison is for data residuals from July averages over the time series 1979-2017. Given
385 the different assumptions underlying the two data sets, the agreement is very good (with an
386 rms difference of 3% for the residuals, and 5% for the actual values of <IWC>).

387 3 Effects of Mean Ice Particle Size



388 The AIR approximation is based on the notion that particle size effects can be ignored.
389 In fact, the particle size (or more accurately, r^3) is a principal ‘driver’ of $\langle IWC \rangle$
390 itself, so it is not obvious that particle size effects may be neglected. Column density
391 also drives IWC, and the dependence of albedo on density adequately captures this
392 part of the variability (albedo is strictly linear in column density). The AIR slope term
393 is proportional to $\frac{r^3}{\sigma_\lambda(r, \Phi)}$ averaged over a distribution of particle sizes, r . Since
394 $\sigma_\lambda(r, \Phi) \sim r^{3-5}$ (where the exponent depends upon Φ) then averaging over many
395 values of r results in a slope term that, in the limit of large number, depends
396 predominantly on Φ . This is an example of “regression to the mean”, and illustrates
397 how the approximation is designed to work for large numbers of clouds. In a fictitious
398 case where the mean cloud particle size is larger in one year than another, but the
399 cloud column number remains the same, the mean albedo would increase according
400 to Eq. (8), resulting in an increase of $\langle IWC \rangle$. We might expect that the slope term
401 would be different in the two cases. Our study with three different data sets shows
402 that the regression slope itself remains almost the same among the three data sets,
403 despite their differing in mean particle size.

404 In fact, Hervig and Stevens (2014) found from SBUV spectral data a small long-term
405 trend in $\langle IWC \rangle$ and in addition a trend in the mean particle size ($+0.23 \pm 0.16$
406 nm/decade). This contributed an additional 20% to the overall long-term trend in
407 $\langle IWC \rangle$. The ignored dependence on mean particle size using the AIR method thus
408 adds a systematic uncertainty in derived $\langle IWC \rangle$ trends, which can be as large as 20%,
409 according to Hervig and Stevens (2014). This error undoubtedly varies inversely with
410 the number of clouds in the averaging process. For example, the number of CIPS
411 observations per PMC season greatly exceeds that of SBUV, so that the error in $\langle IWC \rangle$
412 should be correspondingly smaller.

413 **4 Conclusions**

414 We have described the theoretical basis and accuracy for an approximation for retrieving the
415 average ice water content (IWC) of Polar Mesospheric Clouds (PMC) from measurements of
416 UV albedo at a single scattering angle. This approach provides a continuous set of consistent
417 CIPS measurements of IWC from year to year, regardless of the number of scattering angles
418 for which albedo at a single location is measured. The consistent AIR IWC data base enables
419 robust IWC comparisons throughout the AIM mission, from 2007 to the present. A
420 comparison of IWC derived from the microphysical model and from the CIPS algorithm
421 suggests that CIPS is capable of measuring 84% of the total ice content of PMC (for particle
422 sizes exceeding ~ 23 nm). The accuracy for measuring the total (over all particle sizes) IWC is -
423 $13 \pm 17\%$. The AIR approximation is less accurate for high IWC (>220 g-km $^{-2}$), but very-high
424 mass clouds (IWC > 300 g-km $^{-2}$) are infrequent and do not influence seasonal averages of IWC.
425 The accuracy of the AIR results for ensemble averages has a small systematic dependence on



426 mean particle size- the error depends inversely on the size of the ensemble. The inter-annual
427 and hemispheric variations of IWC derived from CIPS and SBUV measurements throughout an
428 entire 11-year period (2007-2018) will provide detailed information on PMC variability over
429 the recent solar cycle 24.

430 **Figure captions**

431
432 Figure 1. Linear regressions of model PMC albedo versus model PMC ice water content. The
433 black points represent model clouds with $r_{\text{eff}} < 40$ nm. The red points apply to $r_{\text{eff}} > 40$ nm. The
434 blue line is the linear least-squares fit to all points. (a) through (f) are for different scattering
435 angles.

436
437 Figure 2. Errors of ensemble averages, $\langle \text{IWC} \rangle$ using the AIR approximation, taken over all
438 cloud model simulations for conditions of summer solstice. $\langle \text{IWC} \rangle$ is ‘thresholded’ by the
439 variable IWC in the vertical axis, so that $\langle \text{IWC} \rangle$ applies to all values above IWC.

440
441 Figure 3. Differences of IWC derived from the model cloud ‘data’ and the accurate IWC from
442 the model, plotted against the 265-nm albedo (in G units, see text), evaluated at $\text{SA} = 90^\circ$. The
443 error bars are the standard deviations in intervals of 2G.

444
445 Figure 4. Illustration showing how $\text{IWC} = 98 \text{ g}\cdot\text{km}^{-2}$ (horizontal arrow) and $A(90^\circ) = 16 \text{ G}$ (thick
446 downward arrow) are derived from the AIR method from a single measurement of cloud
447 albedo at 60 G and $\text{SA} = 40^\circ$ (upward arrow). Each straight-line plot is calculated from Eq. (9).

448
449 Figure 5. Comparison of CIPS $A(90^\circ)$ (top) and $\langle \text{IWC} \rangle$ (bottom) calculated from the operational
450 (OP) and AIR algorithms. Data points correspond to July northern hemisphere (NH) and
451 January southern hemisphere (SH) averages in a 5-degree latitude bin centered at 70° . Left
452 and right panels are for ascending and descending legs data, respectively.

453
454 Figure 6. Polar projection map of IWC from CIPS, Day 180 (28 June 2012). Left and right panels
455 show the operational IWC product and the AIR result, respectively.

456
457 Figure 7. Same as Fig. 6 except for 28 June 2016.

458
459 Figure 8. Filled circles and dotted line: IWC (AIR) averaged over 1-deg latitude bins centered
460 on 70° (green) and 80° (blue), and over 15 orbits (from which daily averages are derived). Solid
461 line: standard L3C IWC averaged in the same way.

462
463 Figure 9. AIR coefficients for three different sources of IWC and particle size: Model (solid line
464 with open circles), CIPS (solid line), and SOFIE (dashed line).

465
466 Figure 10. Contour plots of the AIR approximations for IWC versus cloud albedo (G) for the
467 three data sources: (a) model, (b) SOFIE, and (c) CIPS.



468

469

470

471

472

473

474

475

476

477

478

479

480

481

482

483

484

485

486

487

488

489

490

491

492

493

494

495

496

497

498

499

500

501

Figure 11. Examples of SOFIE AIR regressions for two (specified) scattering angles, (a) 80° and (b) 110°.

Figure 12. Comparison of annually-averaged northern hemisphere July-averaged residuals ($\langle IWC \rangle$ -long-term mean) derived by two independent methods from SBUV 273 nm albedo data. Black curve: $\langle IWC \rangle$ derived from the AIR approximation. Blue curve: $\langle IWC \rangle$ derived from the same SBUV albedo data, but including mean particle size variations (see text). A three-year smoothing has also been applied.

Data Availability

The CIPS operational PMC data, along with the AIR data, can be found at <http://lasp.colorado.edu/aim/>.

Author Contribution

Author G.T. formulated the AIR approximation, and derived the AIR coefficients from the microphysical model (provided by author C.B.), and from the AIM SOFIE data (<http://sofie.gats-inc.com/sofie/index.php>). Authors J.L. and C.R. calculated the AIR coefficients from the CIPS data.

Disclaimer

The authors declare that they have no conflict of interest.

Acknowledgements

We thank M. DeLand and M. Hervig for providing us with the data used in Fig. 12. We gratefully acknowledge the tremendous effort of the engineering, mission operation and data systems teams whose dedication and skill resulted in the success of the CIPS instrument. AIM is funded by NASA's Small Explorers Program under contract NAS5-03132.

References

Bardeen, C. G., O. B. Toon, E. J. Jensen, M. E. Hervig, C. E. Randall, S. Benze, D. R. Marsh, and A. Merkel: Numerical simulations of the three-dimensional distribution of polar mesospheric clouds and comparisons with Cloud Imaging and Particle Size (CIPS) experiment and the Solar Occultation For Ice Experiment (SOFIE) observations, *J. Geophys. Res.*, 115, D10204, doi:10.1029/2009JD012451, 2010.

Bailey, S.M., Thomas, G.E., Rusch, D.W., Merkel, A.W., Jeppesen, C., Carstens, J.N., Randall, C.E., McClintock, W.E., Russell III, J.M.: Phase functions of polar mesospheric cloud ice as



observed by the CIPS instrument on the AIM satellite, *J. Atmos. Sol.-Terr. Phys.*, **71**, 373-380, doi:10.1016/j.jastp.2008.09.039, 2009.

Baumgarten, G., Chandran, A., Fiedler, J., Hoffman, P., Kaifler, N., Lumpe, J., Merkel, A., Randall, C.E., Rusch, D.W. and Thomas, G. E.: On the horizontal and temporal structure of noctilucent clouds as observed by satellite and lidar at ALOMAR (69N). *Geophys. Res. Lett.*, **39**, L01803, <http://dx.doi.org/10.1029/2011GL049935>, 2012.

Benze, S., Randall, C. E., DeLand, M. T., Thomas, G.E., Rusch, D. W., Bailey, S.M., Russell III, J. M., McClintock, W., Merkel, A. W. and Jeppesen, C.: Comparison of polar mesospheric cloud measurements from the Cloud Imaging and Particle Size experiment and the Solar Backscatter Ultraviolet instrument in 2007, *J. Atmos. Solar-Terr. Phys.*, **71**, 365-372, 2009.

Benze, S., Randall, C.E., Karlsson, B., Harvey, V.L., DeLand, M.T., Thomas, G.E., Shettle, E.P.: On the onset of polar mesospheric cloud seasons as observed by SBUV, *J. Geophys. Res.* **117** <http://dx.doi.org/10.1029/2011JD017350>. D07104, 2012.

DeLand, M. T., Shettle, E. P., Thomas, G. E. and Olivero, J. J.: A quarter-century of satellite PMC observations, *J. Atmos. Sol. Terr. Phys.*, **68**, 9–29, 2006.

DeLand, M. T., and Thomas, G. E.: Updated PMC trends derived from SBUV data, *J. Geophys. Res. Atmos.*, **120**, doi:10.1002/2014JD022253, 2015.

Englert, C. R. and Stevens, M. H.: Polar mesospheric cloud mass and the ice budget: 1. Quantitative interpretation of mid-UV cloud brightness observations, *J. Geophys. Res.*, **112**, D08204, doi:10.1029/2006JD007533, 2007.

Hansen, J. E. and Travis, L.D.: Light scattering in planetary atmospheres, *Space Sci. Rev.* **16**, 527-610, 1974.

Hervig, J. E., Gordley, L.L., Stevens, M. H., Russell III, J. M., Bailey, S. M., and Baumgarten: Interpretation of SOFIE PMC measurements: Cloud identification and derivation of mass density, particle shape, and particle size, *J. Atmos. Sol. Terr. Phys.*, **71**, 316-330, 2009.

Hervig, M. E., and Gordley, L. L.: Temperature, shape, and phase of mesospheric ice from Solar Occultation for Ice Experiment observations, *J. Geophys. Res.*, **115**, D15208, doi:10.1029/2010JD013918, 2010.

Hervig, M. E., and Stevens, M. H.: Interpreting the 35-year SBUV PMC record with SOFIE observations, *J. Geophys. Res. Atmos.*, **119**, 12,689–12,705, doi:10.1002/2014JD021923, 2014.

Hervig, M. E., Berger, U., & Siskind, D. E.: Decadal variability in PMCs and implications for changing temperature and water vapor in the upper mesosphere. *J. Geophys. Res.: Atmos.*, **121**, 2383–2392, <https://doi.org/10.1002/2015JD024439>, 2016.



Lübken, F.-J., Berger, U., and Baumgarten, G.: On the anthropogenic impact on long-term evolution of noctilucent clouds, *Geophys. Res. Lett.*, *45*, <https://doi.org/10.1029/2018GL077719>, 2016.

Lumpe, J.D., Bailey, S.M., Carstens, J.N., Randall, C.E., Rusch, D.W., Thomas, G.E., Nielsen, K., Jeppesen, C., McClintock, W.E., Merkel, A.W., Riesberg, L., Templeman, B., Baumgarten, G., Russell III, J.M.: Retrieval of polar mesospheric cloud properties from CIPS: algorithm description, error analysis and cloud detection sensitivity, *J. Atmos. Sol.-Terr. Phys.*, *104*, 167–196, <http://dx.doi.org/10.1016/j.jastp.2013.06.007>, 2013.

McClintock, W.E., Rusch, D.W., Thomas, G.E., Merkel, A.W., Lankton, M.R., Drake, V.A., Bailey, S.M. and Russell III J.M.: The cloud imaging and particle size experiment on the Aeronomy of Ice in the mesosphere mission: Instrument concept, design, calibration, and on-orbit performance, *JASTP* *71*, 340-355, doi:10.1016/j.jastp.2008.10.011, 2009.

Mishchenko, M.I., Travis, L.D.: Capabilities and limitations of a current Fortran implementation of the T-matrix method for randomly oriented, rotationally symmetric scatterers. *J. Quant. Spectrosc. Radiat. Transf.* *60*, 309–324, 1998.

Rapp, M. and G. E. Thomas: Modeling the microphysics of mesospheric ice particles: Assessment of current capabilities and basic sensitivities, *J. Atmos. Sol.-Terr. Phys.* *68*, 715-744, 2006.

Russell, J. M. III, Bailey, S.M., Gordley, L. L., Rusch, D.W., Hora'nyi, M, Hervig, M. E., Thomas, G. E., Randall, C. E, Siskind, D. E., Stevens, M.H., Summers, M. E., Taylor, M. J., Englert, C. R., Espy, P. J., McClintock, W. E. and Merkel, A.W.: The Aeronomy of Ice in the Mesosphere (AIM) mission: Overview and early science results, *J. Atmos. Sol.-Terr. Phys.* *289*–299, 2009.

Rusch, D. W., Thomas, G.E., McClintock, W., Merkel, A.W., Bailey, S.M., Russell III, J.M., Randall, C.E., Jeppesen, C. and Callan, M.: The cloud imaging and particle size experiment on the aeronomy of ice in the mesosphere mission: Cloud morphology for the northern 2007 season, *J. Atmos. Sol.-Terr. Phys.* *356*–364, 2009.

Thomas, G.E. and McKay, C.P.: On the mean particle size and water content of polar mesospheric clouds. *Planetary Space Science* *33* (10), 1209–1224, 1985.

Thomas, G. E., Olivero, J. J., Jensen, E. J., Schröder, W., and Toon, O. B.: Relation between increasing methane and the presence of ice clouds at the mesopause. *Nature*, *338*, 490–492, 1989.

Thomas, G. E., McPeters, R. D. and Jensen, E. J.: Satellite observations of polar mesospheric clouds by the Solar Backscattered Ultraviolet radiometer: Evidence of a solar cycle dependence, *J. Geophys. Res.*, *96*, 927–939, doi:10.1029/90JD02312, 1991.



Albedo-Ice Regression, SD-WACCM/CARMA microphysical model

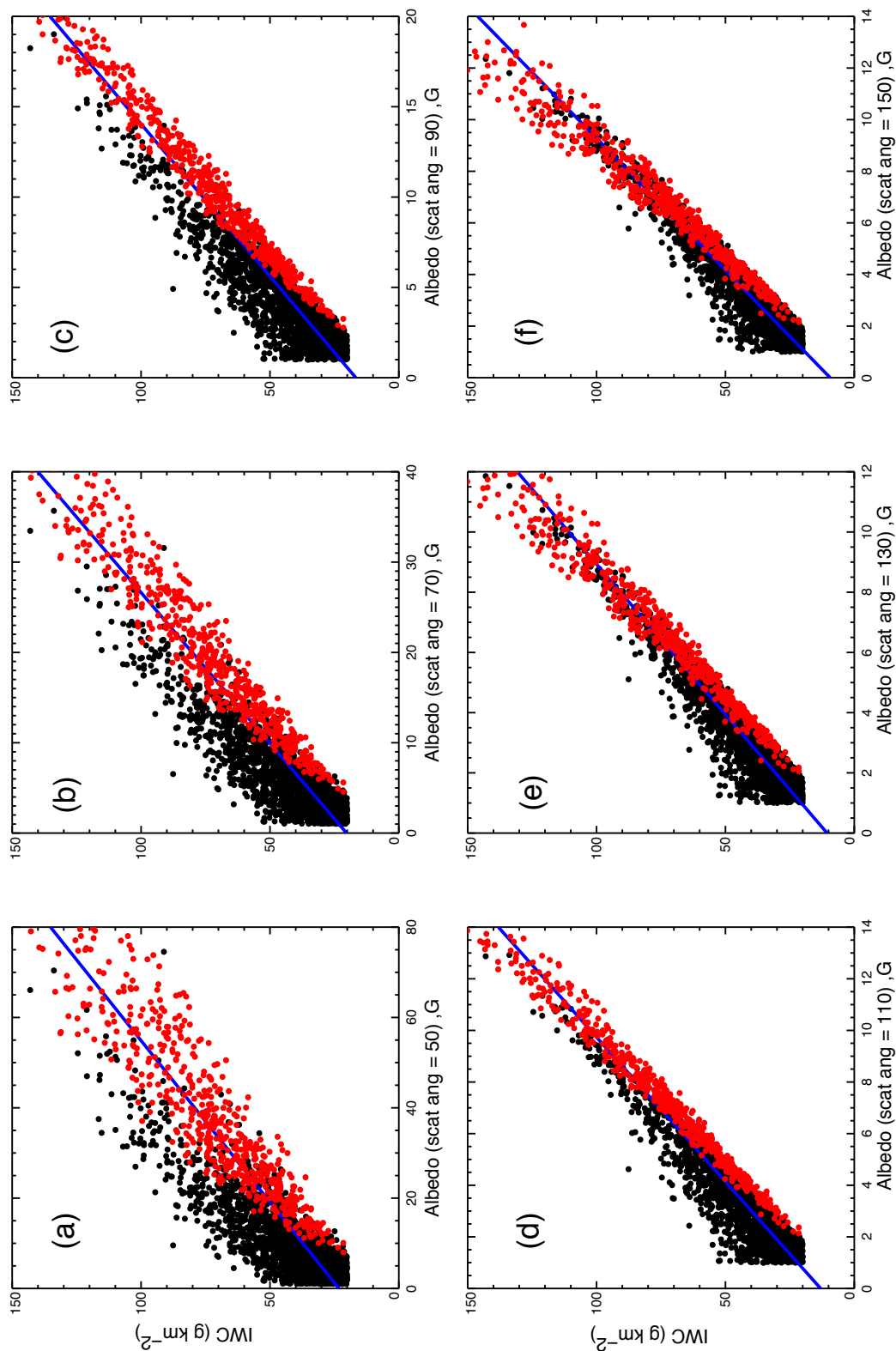


Figure 1

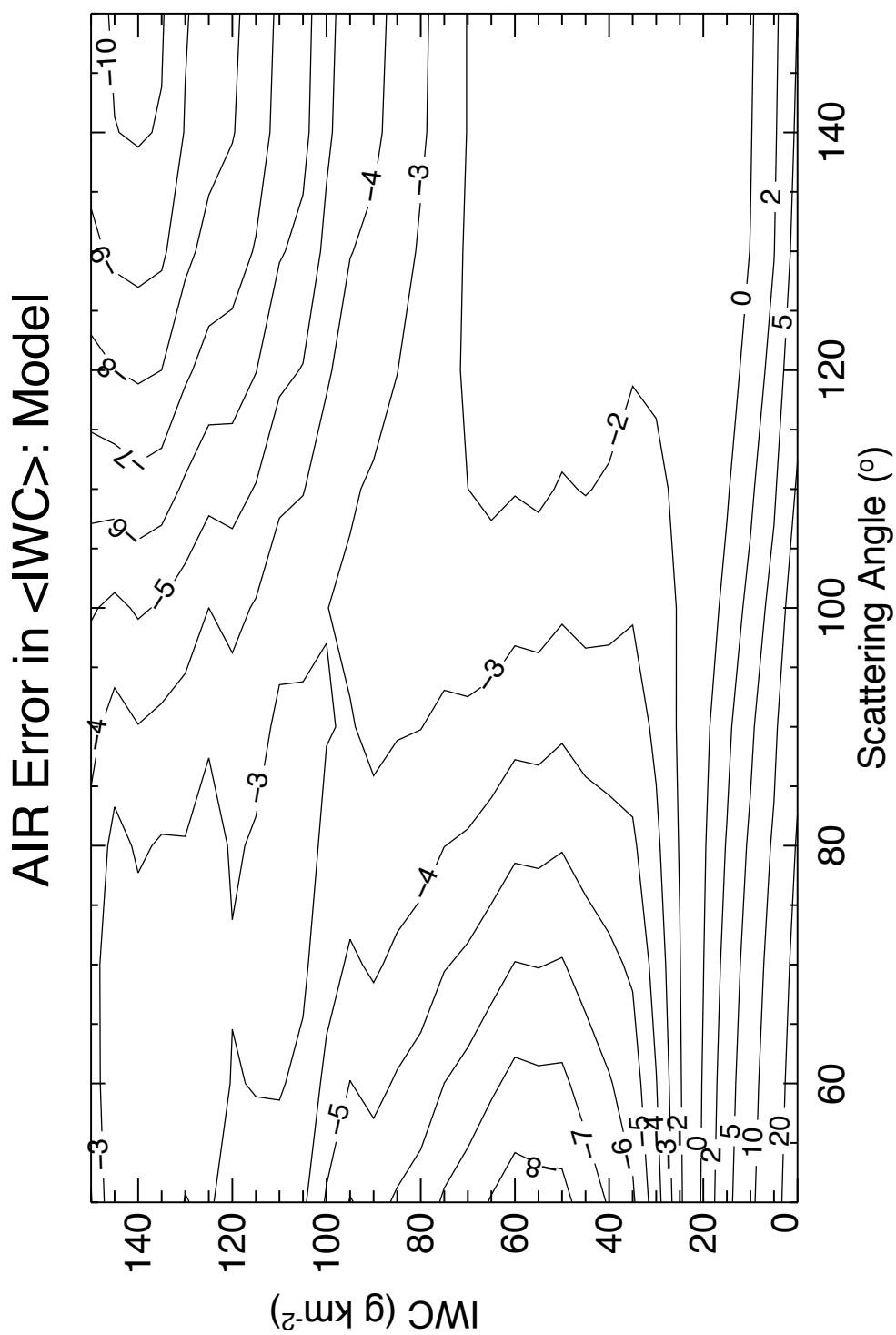


Figure 2

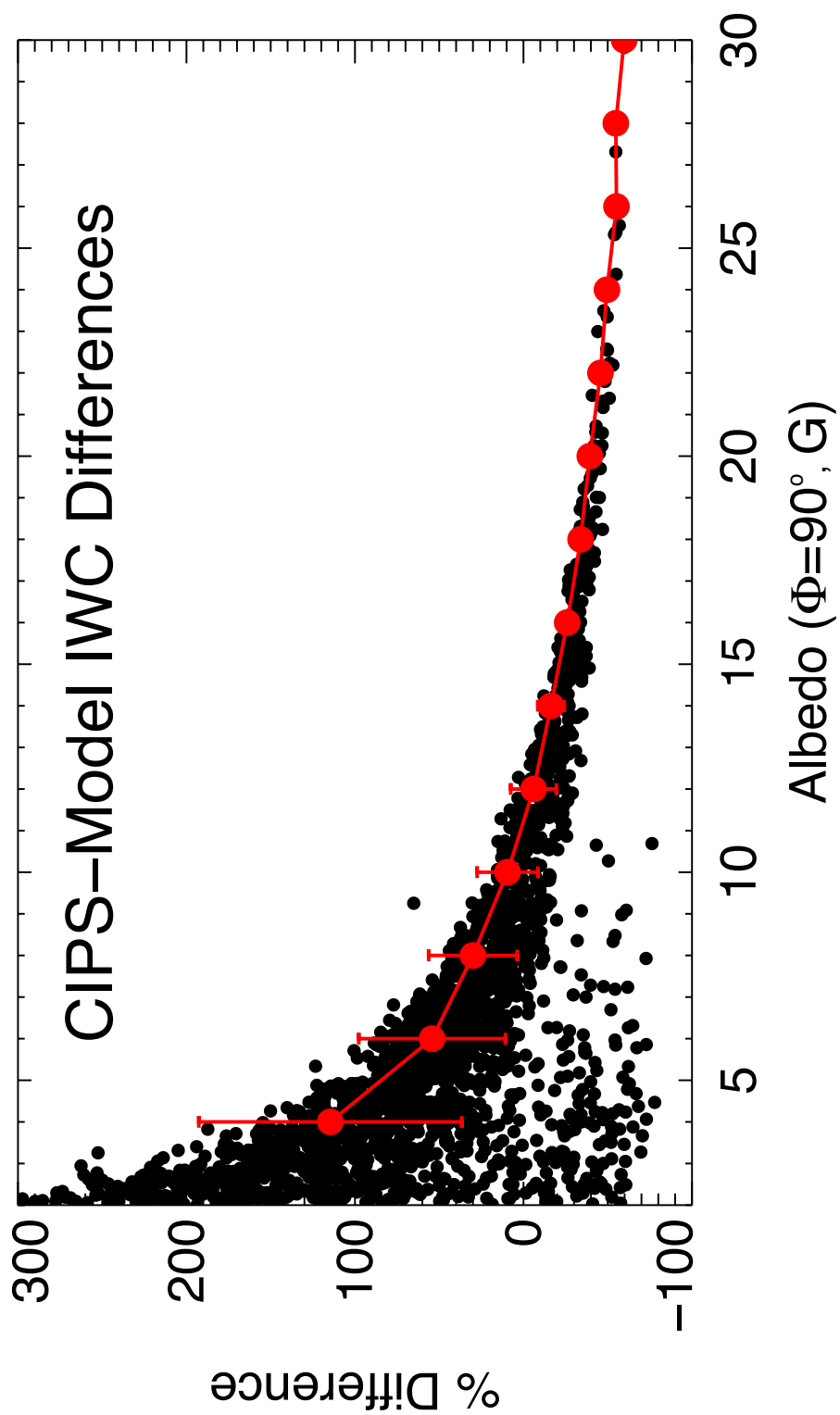


Figure 3

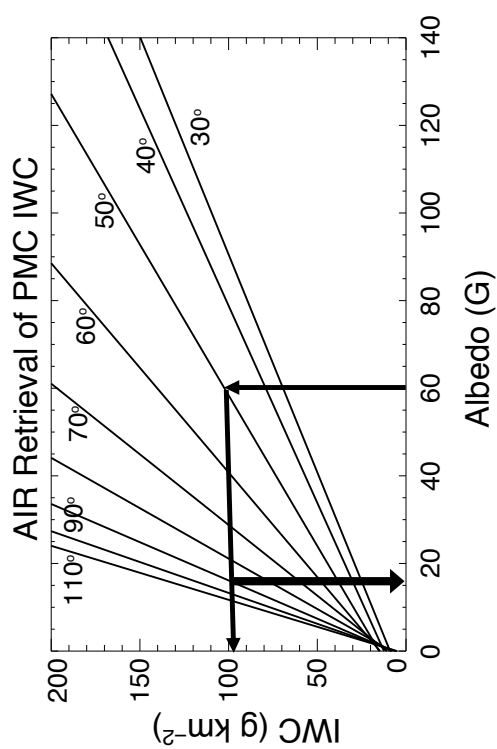
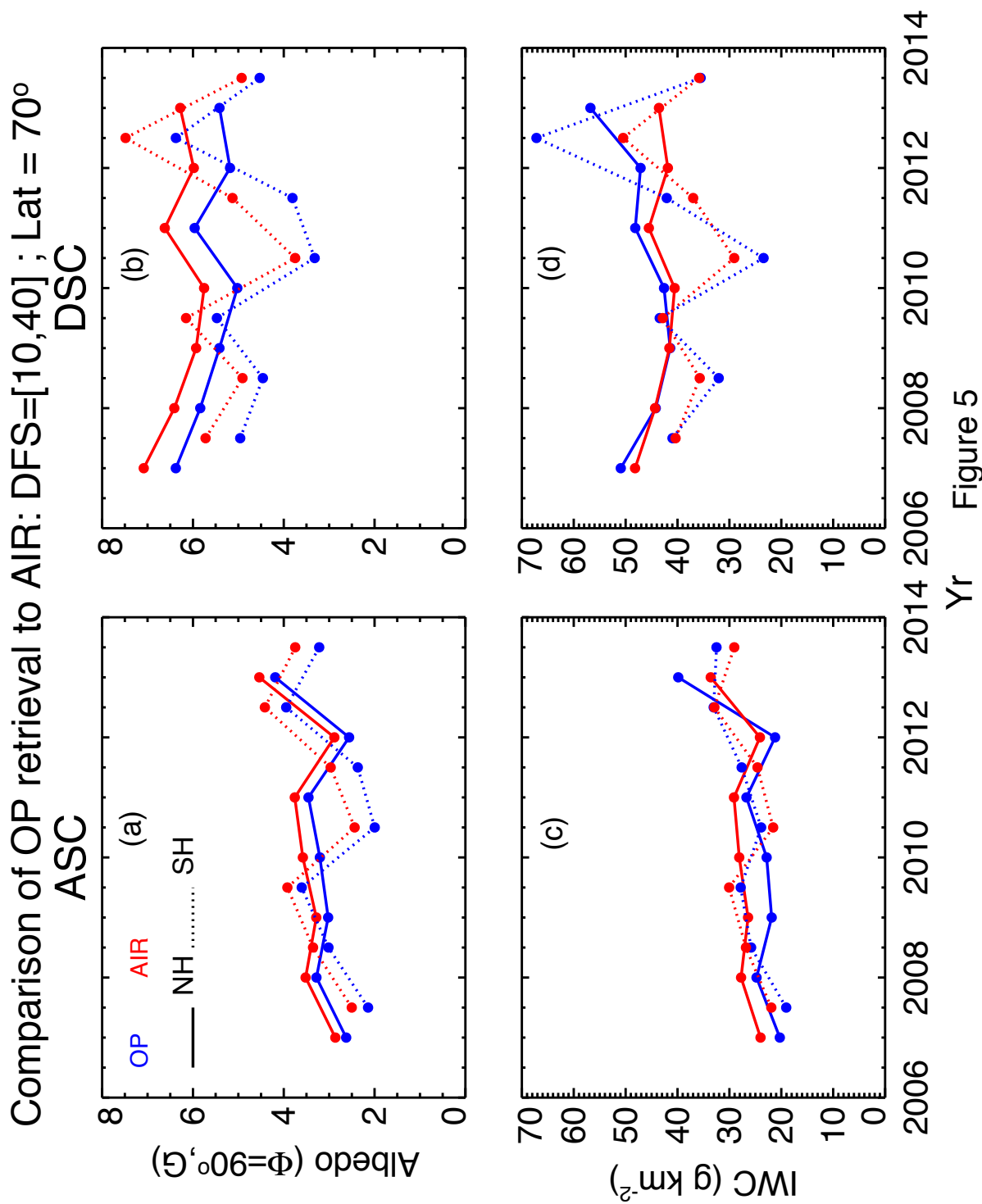
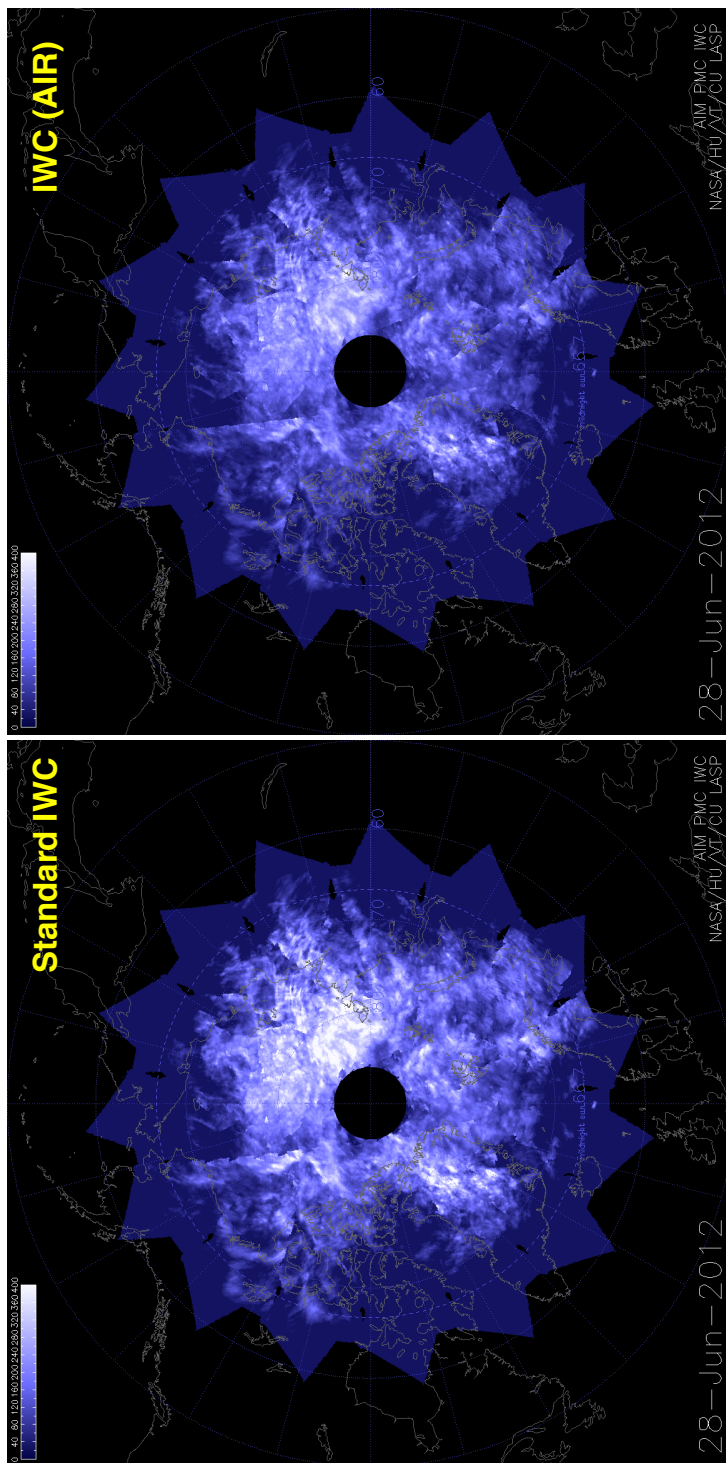


Figure 4





3

23

Figure 6

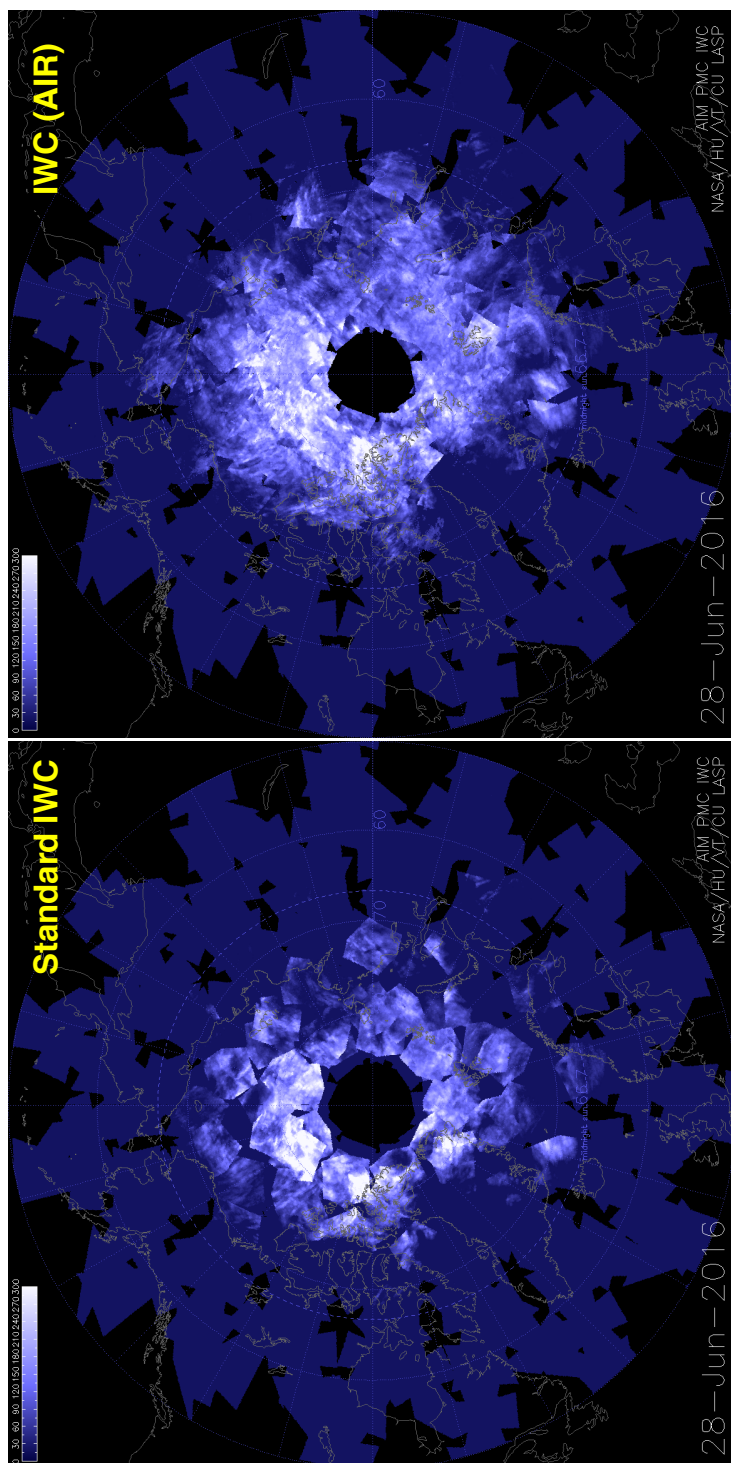


Figure 7

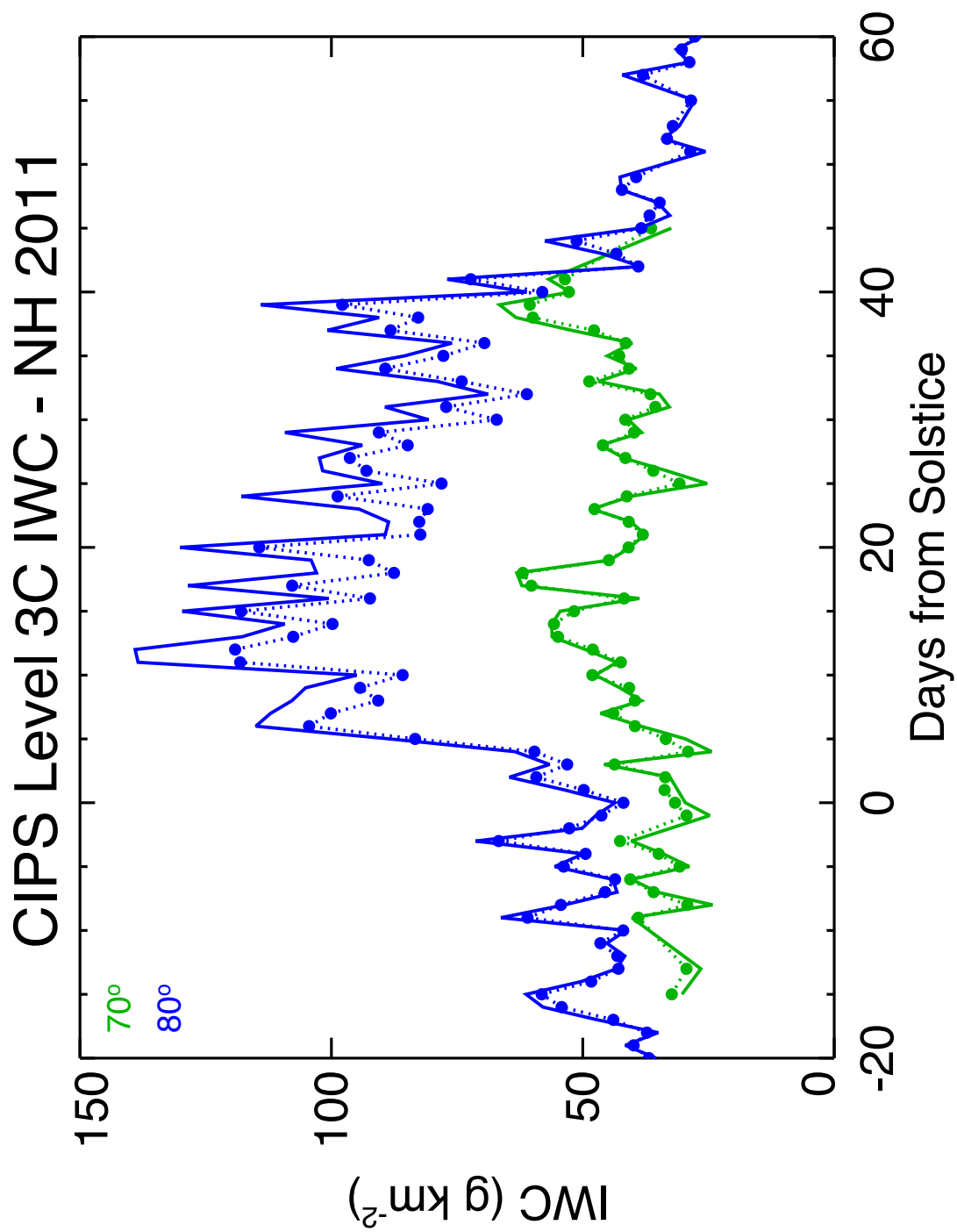


Figure 8

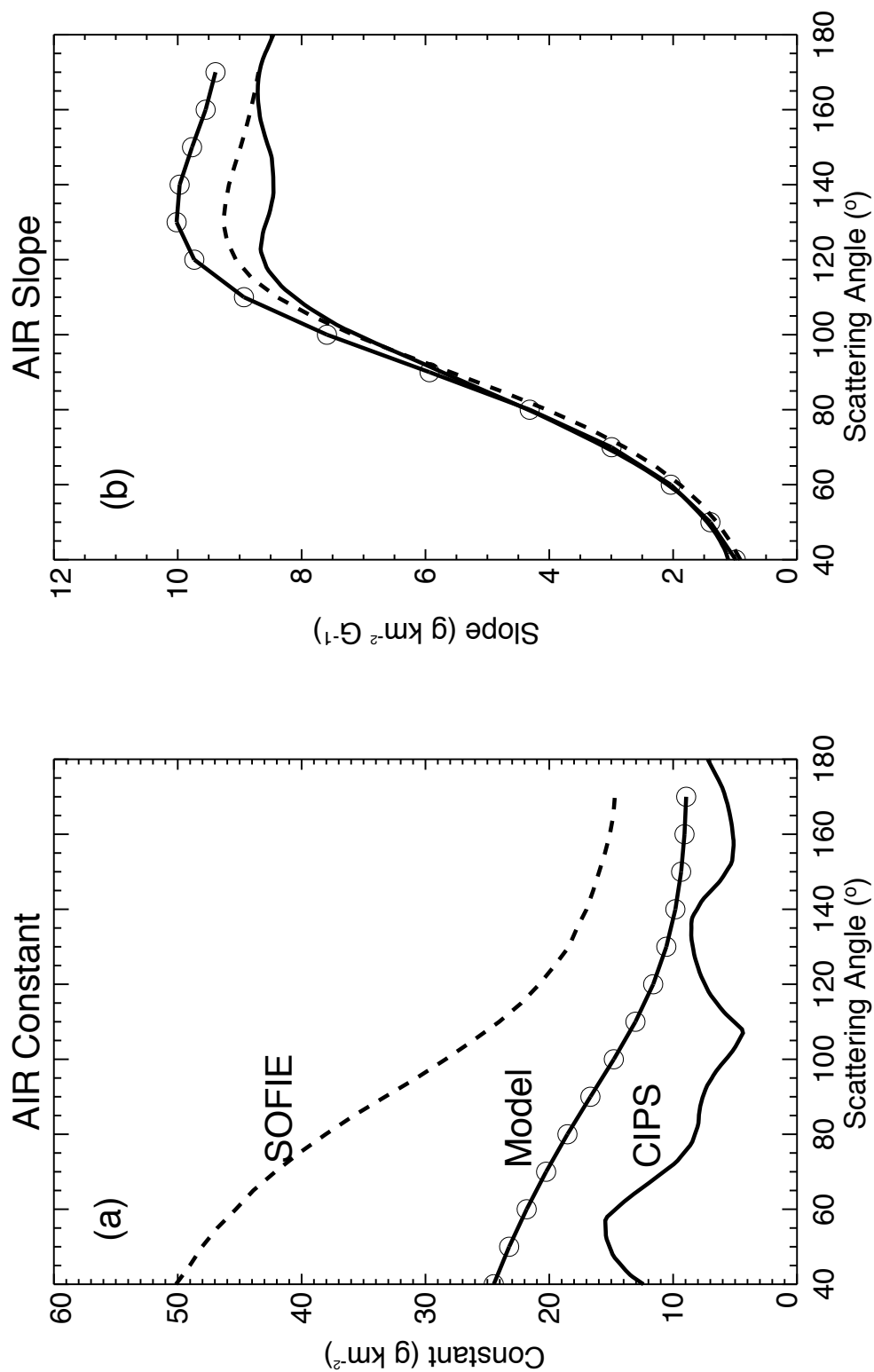


Figure 9

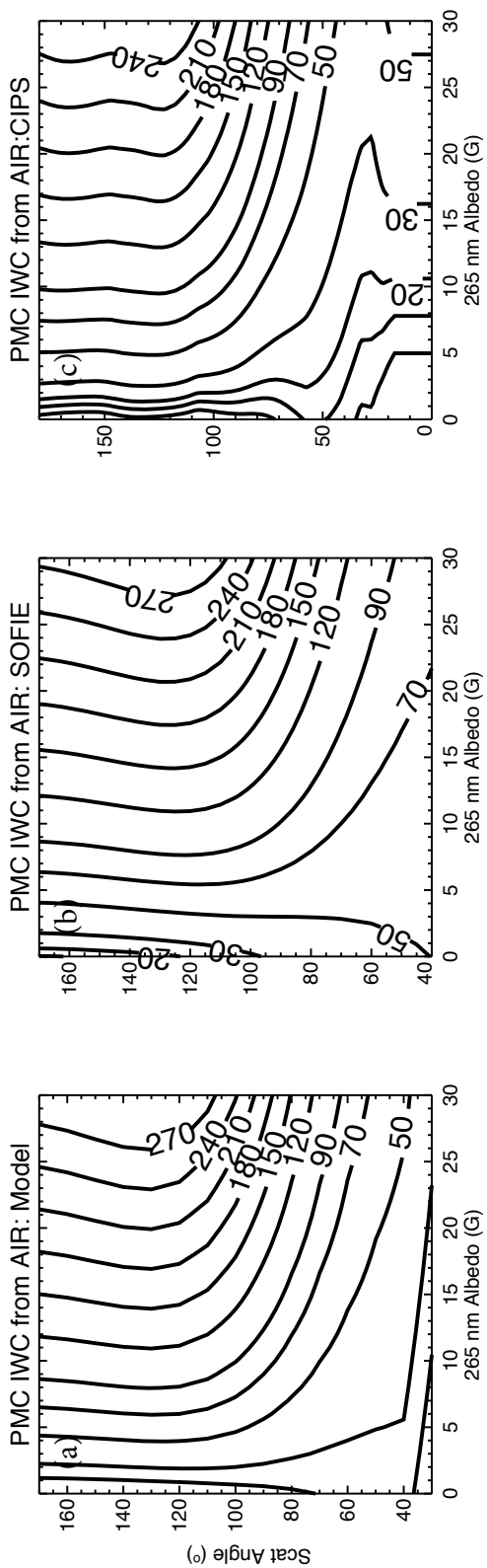


Figure 10

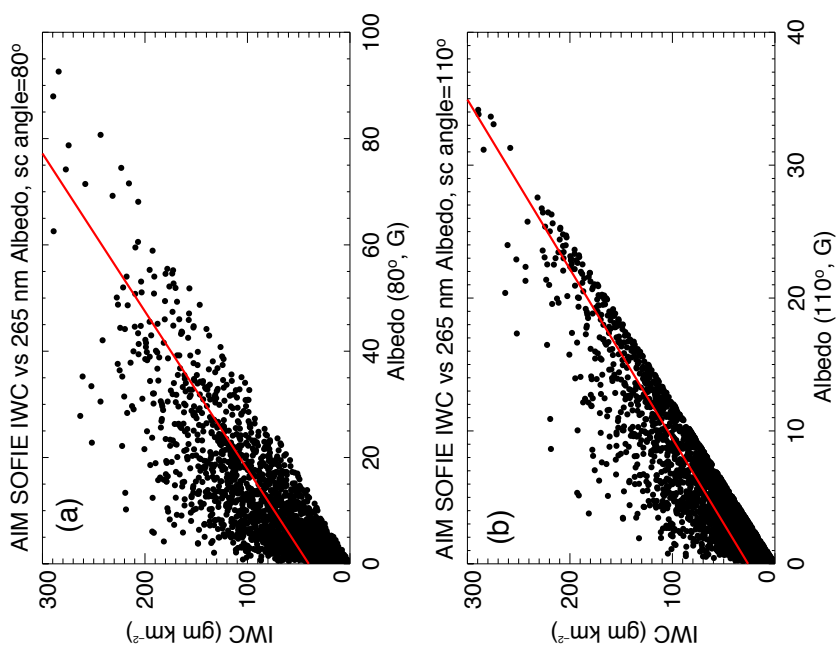


Figure 11

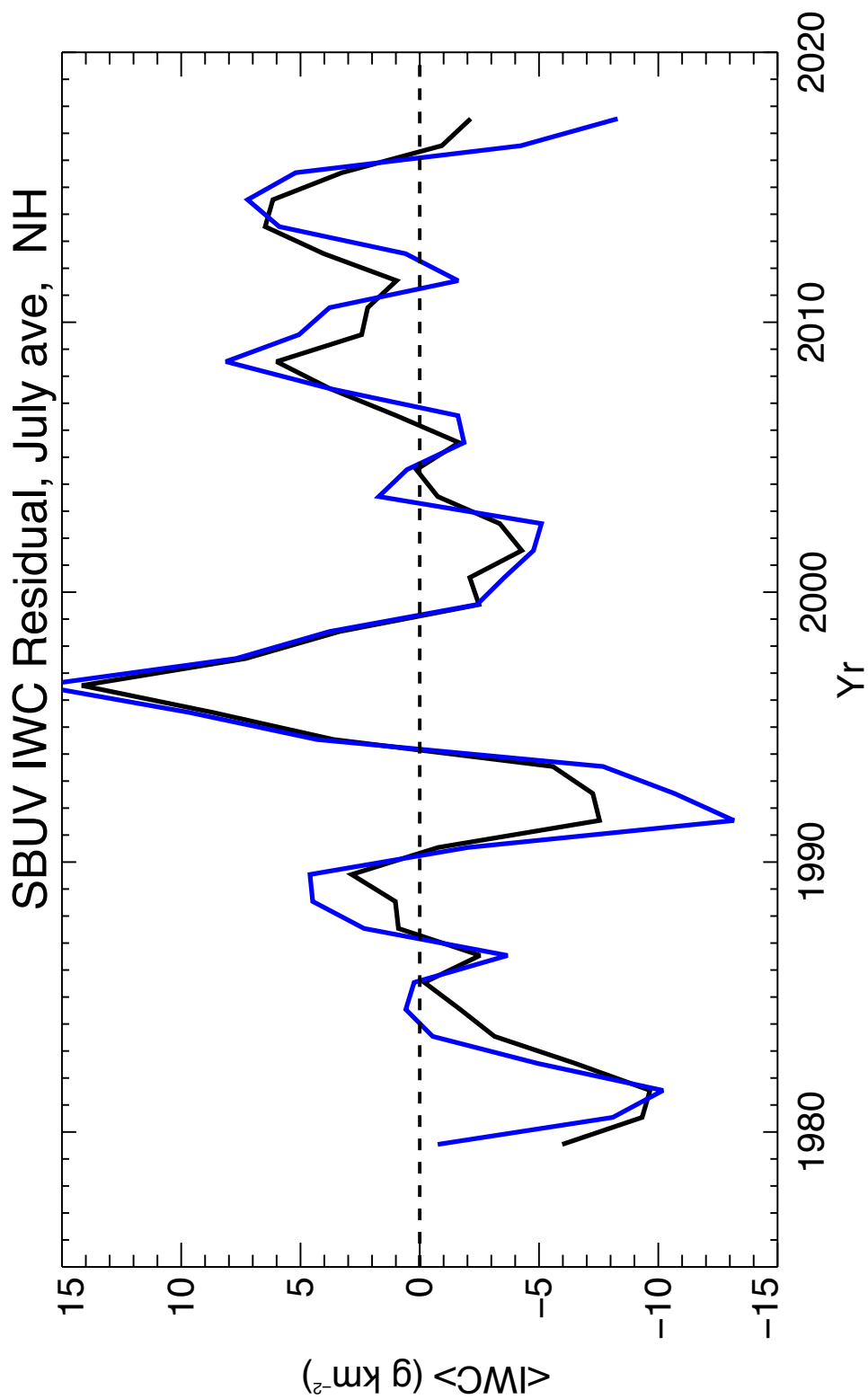


Figure 12